**Germanou, Lefki and Ho, Minh Tuan and Zhang, Yonghao and Wu, Lei (2018) Intrinsic and apparent gas permeability of heterogeneous and anisotropic ultra-tight porous media. Journal of Natural Gas Science and Engineering, 60. pp. 271-283. ISSN 1875-5100 , http://dx.doi.org/10.1016/j.jngse.2018.10.003**

This version is available at https://strathprints.strath.ac.uk/65726/

**Strathprints** is designed to allow users to access the research output of the University of Strathclyde. Unless otherwise explicitly stated on the manuscript, Copyright © and Moral Rights for the papers on this site are retained by the individual authors and/or other copyright owners. Please check the manuscript for details of any other licences that may have been applied. You may not engage in further distribution of the material for any profitmaking activities or any commercial gain. You may freely distribute both the url (https://strathprints.strath.ac.uk/) and the content of this paper for research or private study, educational, or not-for-profit purposes without prior permission or charge.

Any correspondence concerning this service should be sent to the Strathprints administrator: strathprints@strath.ac.uk

The Strathprints institutional repository (https://strathprints.strath.ac.uk) is a digital archive of University of Strathclyde research outputs. It has been developed to disseminate open access research outputs, expose data about those outputs, and enable the management and persistent access to Strathclyde's intellectual output.

Journal of Natural Gas Science and Engineering 60 (2018) 271–283

Contents lists available at ScienceDirect

Journal of Natural Gas Science and Engineering

journal homepage: www.elsevier.com/locate/jngse

# Intrinsic and apparent gas permeability of heterogeneous and anisotropic ultra-tight porous media

Lefki Germanou*, Minh Tuan Ho, Yonghao Zhang, Lei Wu

*James Weir Fluids Laboratory, Department of Mechanical and Aerospace Engineering, University of Strathclyde, Glasgow, G1 1XJ, UK*

ARTICLE INFO

*Keywords:*
Rarefied gas dynamics
Porous media
Gas permeability
Slip factor

ABSTRACT

Accurate prediction of unconventional gas production requires deep understanding of the permeability of complex rock samples. Several predictive expressions of permeability, which include either simplifications of the porous media structure or the flow mechanisms, have been proposed recently. The main objective of this research is to quantify the impact of solid matrix complexity on both intrinsic and apparent permeability. To this end, numerous two-dimensional random porous media structures are constructed using the quartet structure generation set algorithm. Parametric and statistical analysis reveals the importance of the specific surface area of pores, tortuosity, heterogeneity and degree of anisotropy. Special focus is given to the directional dependency of the permeability on isotropic and anisotropic geometries, considering the great impact of anisotropy on the laboratory evaluation of permeability data and the anisotropic nature of shale rocks. Simulation results, for the same value of porosity, clearly indicate the drastic improvement of permeability due to the reduction of specific surface area of pores and their height to width ratio. This suggests that rock matrix complexity has significant impact on permeability and should not be neglected while forming permeability formulations for porous media. Finally, the results of the apparent permeability, obtained by solving the gas kinetic equation, are taken into consideration to demonstrate the enhancement ratio, slip factor and their correlation with the aforementioned parameters. Semi-analytical expressions for intrinsic and apparent permeability, considering continuum and slip flow respectively, are derived. The proposed formulations, suitable for both isotropic and anisotropic structures, have the advantage of not entailing any numerical or experimental data as input.

## 1. Introduction

Shale gas has attracted significant global interest due to its successful production in the United States, favoured by the recent development of economic extraction technologies. However, “shale gas revolution” is not equally advanced in other regions of the world, where geological conditions might be more complex and hence, the extraction cost is high. Therefore, to make global exploitation of shale gas reserves possible, accurate monitoring, prediction and optimization of the production is indispensable. Typically, this is achieved through reservoir-scale fluid flow simulations in the order of kilometres, which require input parameters, such as porosity and permeability, that characterize the rock formation. Shale is considered a fine-grained sedimentary rock of ultra-low permeability due to its nano-pores. Macroscopic behaviour is thus directly linked to the internal micro-structure, which in the case of shale is quite complex and presents heterogeneous features (Wang et al., 2017). Under these circumstances, understanding the multi-scale transport of shale gas requires firstly thorough examination of the reservoir's micro-structure. This has been made possible by the recent development of imaging techniques. For instance, Focused-Ion-Beam/Scanning Electron Microscope imaging can provide two-dimensional (2D) or 3D digital images with a resolution as high as 6.5 nm whereas the state-of-the-art Helium-Ion-Microscope can even approach 0.5 nm resolution (Wu et al., 2017b).

Numerical simulation can be directly applied on the above imaging models to reveal the gas transport mechanism. However, this is not an easy task since the computational fluid dynamics based on continuum approach fail in the area of non-equilibrium gas dynamics. The primary reason is that the molecular nature of the gas can no longer be ignored when its mean free path becomes comparable to the characteristic length of the flow. For example, the Navier-Stokes equations (NSEs) under-predict the gas flow rate through carbon nanotubes by several orders of magnitude (Holt, 2006). At the micro/nano-scale, collisions between gas molecules are too infrequent to fully thermodynamically equilibrate gas, causing velocity slip and temperature jump at solid surfaces, and Knudsen layer of non-linear stress/strain-rate behaviour

* Corresponding author.
*E-mail address:* lefki.germanou@strath.ac.uk (L. Germanou).

https://doi.org/10.1016/j.jngse.2018.10.003
Received 12 July 2018; Received in revised form 5 October 2018; Accepted 10 October 2018
Available online 12 October 2018
1875-5100/ © 2018 The Authors. Published by Elsevier B.V. This is an open access article under the CC BY license (http://creativecommons.org/licenses/BY/4.0/).

(Gad-el Hak, 1999). For methane and carbon dioxide in an unconventional reservoir, with pressures up to several hundred bars, the gas flow through nano-pores is in the slip and transition regimes (Kazmouz et al., 2016). In all these cases, gas flow cannot be assumed to be in quasi-equilibrium. A direct consequence of the gas rarefaction is that the apparent gas permeability $k_a$ is larger than the intrinsic (Darcy) permeability $k_{in}$ and rises as the mean gas pressure decreases (Klinkenberg, 1941). The intrinsic permeability depends on the void space and solid surface characteristics, while the apparent gas permeability additionally takes into account the gas pressure (Ghassemi and Pak, 2011).

Many researchers have focused on deriving analytical formulations to describe the apparent permeability of reservoir rocks, most of them based on the straight tube simplification (Civan, 2010; Javadpour, 2009; Lin et al., 2017). Another modelling approach uses the fractal dimension and tortuosity to account for the roughness of pore surfaces and sinuous flow paths respectively (Darabi et al., 2012; Zhang et al., 2015). A latter concept is the gas permeability upscaling from a single pore to a pore network (Ghanbarian and Javadpour, 2017). The above models estimate some of their parameters, such as Darcy permeability, tortuosity, and fractal dimension of surface, through experiments. Consequently, the literature provides a large amount of apparent gas permeability models which focus on the transport phenomena ignoring the full extend of rock matrix complexity.

On the other hand, it is well-documented by many researchers that pore size and geometry have a notable effect on the proportion of diffusion in total flow rate (Javadpour, 2009; Ren et al., 2016; Singh et al., 2014). Additionally, many models incorporating the simplification of the porous medium as a bundle of straight cylindrical tubes are proven to produce contradictory results compared to experimental observations of ultra-tight porous media. Specifically, in our recent paper (Wu et al., 2017a), it is found that Klinkenberg's experimental results can only be explained if flow tortuosity is considered. Thus, the porosity, specific surface area, tortuosity and anisotropy are some of the matrix properties that play a significant role in the overall production performance.

This study aims to investigate the impact of the aforementioned parameters on both intrinsic and apparent permeability and propose new appropriate permeability formulations. The rest of this paper is organized as follows. In Section 2, the details of the simulated porous media are mentioned, along with the equations that govern the flow and the numerical schemes utilized. In Section 3, the simulation results are discussed, analysing the role of porosity, specific surface area, tortuosity and anisotropy on intrinsic permeability. Additionally, a new formulation for intrinsic permeability, based on an existing analytical formula and the simulation results of this work, is presented. Later, in Section 4, the simulation results for apparent permeability are presented and the impact of the structural parameters, reflected on the enhancement ratio and the slip factor, is discussed in detail. Moreover, the proposed formulation is extended to account for slip flow, thus providing apparent permeability. Finally, the conclusions of this work are given in Section 5.

## 2. Model description

The present study, focusing on the morphological complexity of porous media, aims to investigate the contribution of the structural properties in gas permeability. To this end, numerous flow simulations are performed and analysed on various 2D random micro-porous media generated by the Quartet Structure Generation Set (QSGS) method (Wang et al., 2007). This method allows shale structure reconstruction by a set of parameters that control the internal porous structure, in a way that morphological features resemble the ones of the shale matrix (Chen et al., 2015b; Wang et al., 2007).

### 2.1. Geometry generation

In particular, a two-phase QSGS process, where the solid is the growing phase and the pores are the non-growing phase, is applied. The controlling parameters are the volume fraction $P$, the core distribution probability $c_d$, and the directional growth probability $D_i$, all within [0,1]. The volume fraction is more commonly expressed as porosity $\varepsilon$, where ($\varepsilon = 1 - P$). The core distribution probability indicates the density of the cores from which the solid particles are formed: when the porosity is fixed, the smaller the value of $c_d$, the less the number of solid islands. Finally, the directional growth probability indicates the way a core cell expands and forms a solid particle in order to reach the desired volume fraction. The cell expands along the $i$ direction (four main and four diagonal directions) according to the value of $D_i$. Thus, adjusting $D_i$ in the eight directions appropriately, controls the degree of anisotropy. The QSGS process follows the steps below.

1. Randomly distribute the cores in the grid based on a core distribution probability $c_d$, whose value is far less that the desired volume fraction $P$. Each cell is assigned a random number; the cells whose random number is less than $c_d$ are selected as cores.
2. Enlarge the growing phase according to the given directional growth probability $D_i$. The neighbouring cells of the existing solid elements are assigned new random numbers. The neighbouring cell in direction $i$ will belong to the solid phase if its random number is less than $D_i$.
3. The previous step is repeated until the volume fraction reaches the desired value $P$.

Some schematics of the porous media generated by the QSGS method are shown in Fig. 1. In each figure, one parameter varies and the rest two are kept fixed. All the structures used in the present study consist of a numerical grid of $N_x \times N_y = 1000 \times 1000$ nodes.

Due to the random fluctuations occurring during the generation procedure, the geometries produced utilizing the same set of controlling parameters do not have identical morphological features. Consequently, the calculated permeability for these geometries is not the same, but it fluctuates around a mean value. It should be noted that the resulting geometries using the QSGS method often include occluded pores inside the solid impermeable particles which are not connected to the main void space. In order to eliminate these unrealistic fluid cells a pre-processing treatment of the binary matrix was applied using the software MATLAB. As a result, the final structure has a porosity smaller than the nominal one depending on the amount of the occluded pores. To compensate for these differences in the produced geometries and thus the resulting permeability values, for every set of parameters (configuration) 10 porous structures are generated. Both the mean values and the deviation of the computed quantities are taken into account.

### 2.2. Governing equations and numerical methods

#### 2.2.1. Navier-Stokes equations

In order to determine the intrinsic permeability, the pore-scale flows of these structures are evaluated using the finite volume method implemented in the open-source platform OpenFOAM. The binary matrix generated by the QSGS method, after the filling of the occluded pores, is transformed into a mesh representing the pore space of the sample. For the numerical solution of the NSEs, this is achieved using snappyHexMesh, a native mesher of the OpenFOAM CFD toolbox. The result is a hexahedral mesh perfectly matching the aforementioned final structure and image resolution. Note that the original geometry is extended by four fluid layers at the inlet and outlet so that the periodic boundary conditions are applicable.

The incompressible single phase flow is governed by the NSEs characterized by low Reynolds numbers:

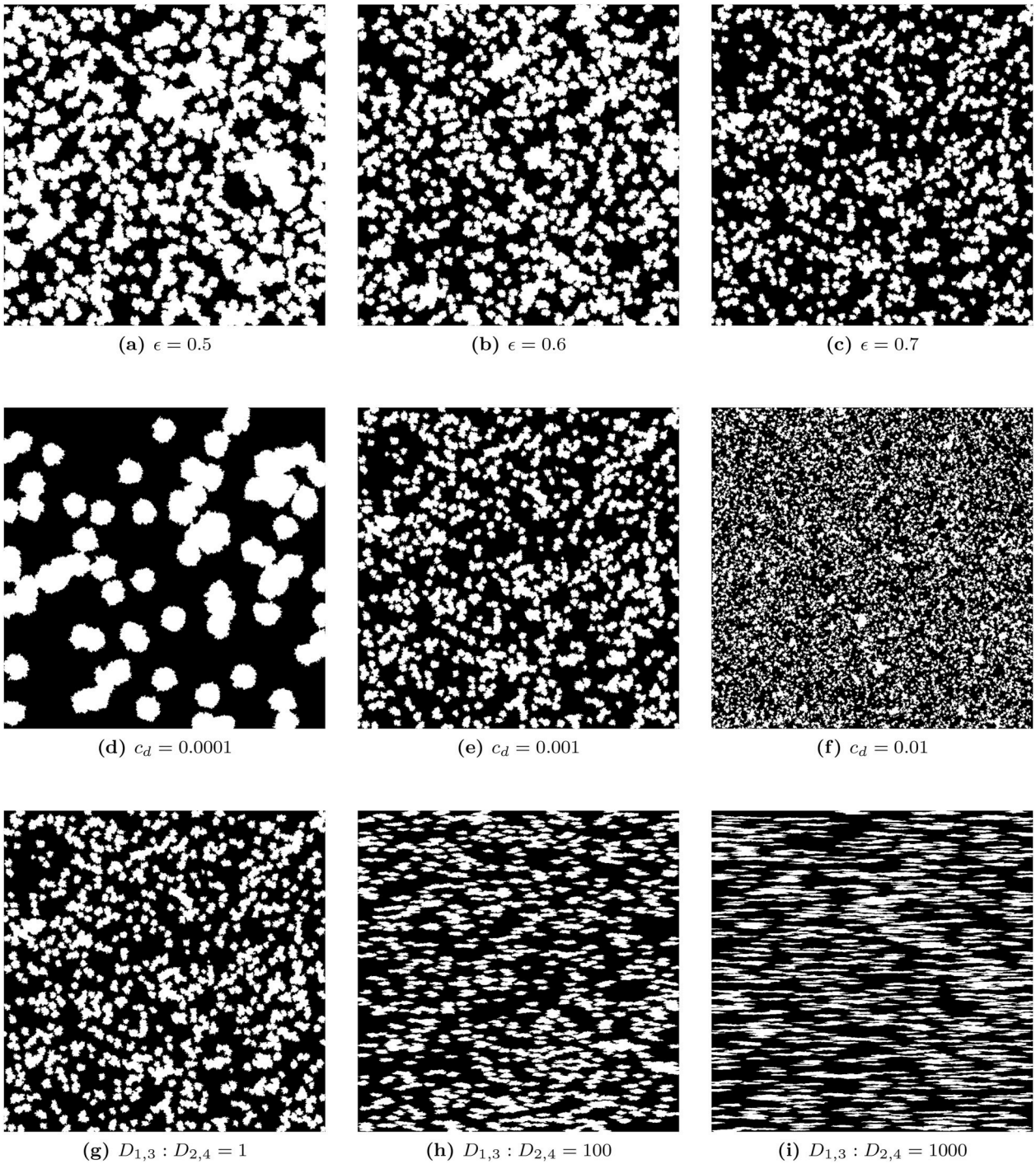


**Fig. 1.** Typical geometries generated by the QSGS algorithm. First row: the core distribution probability is $c_d$ = 0.001 and the ratio of the directional growth probability is $D_{1,3}$: $D_{2,4}$ = 1, while the porosity $\epsilon$ is varied. Second row: ε = 0.7 and $D_{1,3}$: $D_{2,4}$ = 1. Third row: ε = 0.7 and $c_d$ = 0.001. The data of the 400 QSGS geometries within this publication can be freely accessed at http://dx.doi.org/10.17632/mdhxr976vg.1.

$$\nabla \cdot \boldsymbol{u} = 0, \tag{1a}$$

$$(\boldsymbol{u} \cdot \nabla)\boldsymbol{u} - \nu \nabla^2 \boldsymbol{u} = -\nabla p, \tag{1b}$$

where $\boldsymbol{u}$ is the flow velocity, $\nu$ is the kinematic viscosity and $p$ is pressure. The solver used is based on the Semi-Implicit Method for Pressure Linked Equations (SIMPLE) algorithm and all the discretization schemes are second order. Periodic boundary conditions are imposed at the inlet/outlet, symmetry (no-flux condition) at the lateral walls and no-slip at the solid surfaces (Wu et al., 2017a). The fluid is forced to move in the desired direction by adding a pressure gradient source term in the momentum equation while assuring $Re < 1$. This setup, due to the periodicity imposed, is a priori anticipated to result in a good approximation of the real permeability (Guibert et al., 2015). The alternative setup of fixed pressure in the inlet and outlet to drive the flow (mimics the experimental condition) is also tested and the calculated permeabilities have a small deviation in the order of 1%. In both cases, the intrinsic permeability for laminar flows is calculated according to Darcy law:

$$\boldsymbol{q} = \frac{k_{in}}{\mu} \nabla p, \tag{2}$$

where $\boldsymbol{q}$ is the mass flux, $\nabla p$ is the pressure gradient, and $\mu$ is the shear

viscosity of the fluid.

#### 2.2.2. Gas kinetic theory

The Knudsen number is a main indicator of the degree of thermodynamic non-equilibrium of a flow and thus it is the characteristic parameter for gas flow in micro-scale porous media. It is usually defined as the ratio of the mean free path of gas molecules to the characteristic flow length $L$:

$$Kn = \frac{\lambda}{L}, \quad \text{and} \quad \lambda = \frac{\mu(T_0)}{\bar{p}}\sqrt{\frac{\pi R T_0}{2}}, \tag{3}$$

where $\mu(T_0)$ is the shear viscosity of the gas at a reference temperature $T_0$, $\bar{p}$ is gas pressure, and $R$ is the gas constant.

Based on $Kn$, gas flows can be classified into four regimes: continuum flow ($Kn \leq 0.001$) in which the NSEs are valid, slip flow ($0.001 < Kn \leq 0.1$) where the NSEs need appropriate velocity-slip boundary conditions, transition ($0.1 < Kn \leq 10$) and free molecular flows ($Kn > 10$) where the continuum assumption breaks down. In rarefied gas flows, the permeability depends not only on the structure of porous media, but also on the gas pressure, or equivalently, the Knudsen number. The apparent permeability is augmented compared to the intrinsic one as firstly expressed by Klinkenberg (1941) as follows:

$$k_a = k_{in}\left(1 + \frac{b}{\bar{p}}\right), \tag{4}$$

where $b$ is the slip factor which is usually not a constant (Wu et al., 2017a).

Since the apparent gas permeability is a result of gas rarefaction, the gas kinetic theory is adopted to describe the shale gas transport in ultra-tight porous media. Here we use the following linearized BGK model equation, which can be viewed as the relaxation-time approximation of the Boltzmann equation (Bhatnagar et al., 1954):

$$\boldsymbol{v}\frac{\partial h}{\partial \boldsymbol{x}} = \frac{\sqrt{\pi}}{2Kn}\left[\varrho + 2\boldsymbol{u}\cdot\boldsymbol{v} + \tau\left(|\boldsymbol{v}|^2 - \frac{3}{2}\right) - h\right], \tag{5}$$

where $h(x_1, x_2, \boldsymbol{v})$ is the velocity distribution function deviated from the Maxwellian equilibrium distribution function $f_{eq} = \exp(-|\boldsymbol{v}|^2)/\pi^{3/2}$, $\boldsymbol{v} = (v_1, v_2, v_3)$ is the three-dimensional molecular velocity normalized by the most probable molecular speed $v_m = \sqrt{2RT_0}$ and $\boldsymbol{x} = (x_1, x_2, x_3)$ is the spatial coordinate normalized by the length $L = AB$ of the computational domain shown in Fig. 2. Macroscopic quantities appearing in the right-hand side of Eq. (5) are the perturbed number density of gas molecules $\varrho = \int h f_{eq}\, d\boldsymbol{v}$, the flow velocity $\boldsymbol{u} = (u_1, u_2, u_3) = \int (v_1, v_2, v_3) h f_{eq}\, d\boldsymbol{v}$, and the perturbed temperature $\tau = \frac{2}{3}\int |\boldsymbol{v}|^2 h f_{eq}\, d\boldsymbol{v} - \varrho$. Note that Eq. (5) is valid when the porous medium is so long that the pressure gradient is small, namely, $|L dp/p dx_1| \ll 1$ with $p$ being the local gas pressure and $x_1$ is the flow direction.

The kinetic equation (5) has to be supplied with appropriate boundary conditions. Suppose the pressure gradient is applied along the $x_1$ (horizontal) direction, on the inlet and outlet of the computational domain ABCD in Fig. 2 and periodic condition for the flow velocity is used (Sharipov and Graur, 2012): when $v_1 \gtrless 0$, we have $h(\mp 0.5, x_2, v_1, v_2, v_3) = \pm 1 + h(\pm 0.5, x_2, v_1, v_2, v_3)$. At lines AB and CD the specular reflection boundary condition is used to account for spatial symmetry. That is, when $v_2 > 0$ we have $h(x_1, 0, v_1, v_2, v_3) = h(x_1, 0, v_1, -v_2, v_3)$, when $v_2 < 0$ we have $h(x_1, 0.5, v_1, v_2, v_3) = h(x_1, 0.5, v_1, -v_2, v_3)$. Finally, at the solid surface, the diffuse boundary condition is used (Maxwell, 1879): $h(\boldsymbol{v}) = \frac{2}{\pi}\int_{v_n' < 0} |v_n'| h(\boldsymbol{v}') \exp(-|\boldsymbol{v}'|^2) d\boldsymbol{v}'$, where $\boldsymbol{n}$ is the outer normal vector of the solid surface. This boundary condition assumes that, after collision with the surface, a gas molecule is reflected diffusely (i.e. reflected towards every direction with equal probability, in a Maxwellian velocity distribution).

The apparent gas permeability, which is normalized by $L^2$, is calculated by

$$k_a = 2\sqrt{\frac{1}{\pi}}\, Kn G_P, \tag{6}$$

where $G_p = 2\int_0^{1/2} u_1(x_2) dx_2$ is the dimensionless mass flow rate.

In the numerical simulations of low-speed rarefied gas flows, the linearized BGK equation is often used, (Varoutis et al., 2009), which herein is solved by the Discrete Velocity Method (DVM). A mesh of double resolution is utilized to enhance accuracy, particularly when $Kn$ is small. Apart from the spatial discretization, the molecular velocity space $\mathbf{v}$ is also discretized. Since the non-equilibrium effects are related to the high-order moments of the velocity distribution function, a higher-order quadrature must be used to capture the rarefaction effect accurately. In general, the larger the Kn number, the larger the variations and discontinuities of the velocity distribution function $h$. Thus, the number of discrete velocities should rise accordingly (Su et al., 2017). Using DVM, in this study $v_1$ and $v_2$ in the BGK equation are approximated by the $8 \times 8$ Gauss–Hermite quadrature when $Kn < 0.01$ and the Newton-Cotes quadrature with $22 \times 22$ non-uniform discrete velocity points for higher Kn numbers (Wu et al., 2017a). The $v_3$ variable can be safely ignored in this linearized flow.

## 3. Intrinsic permeability

### 3.1. Computed quantities

To evaluate the influence of several morphological aspects on the permeability of micro-porous media, some relevant quantities are taken into consideration. First, streamlines in porous media are usually not

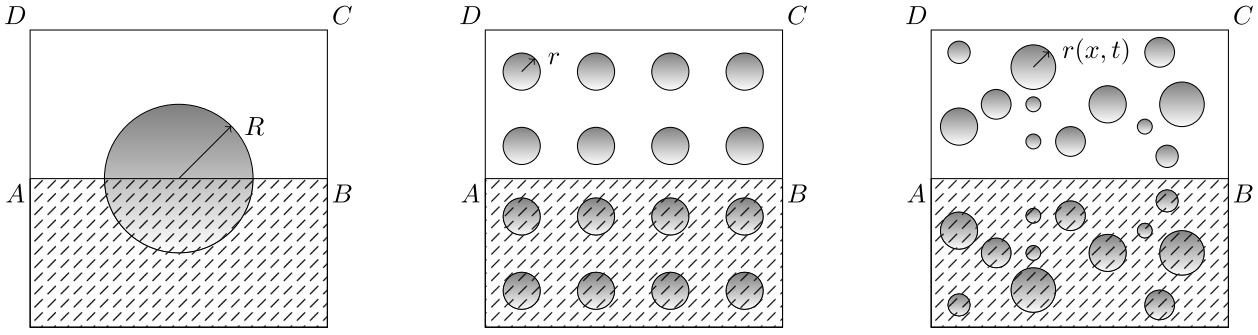


**Fig. 2.** Schematic representation of a two-dimensional porous medium. A porous medium consisting of a periodic array of discs can be generated using the concept of the unit rectangular cell *ABCD*; applying periodic boundary condition at sides *AD* and *BC* and symmetrical boundary condition along sides *AB* and *CD*, respectively. The rectangle *ABCD* is the computational domain where the length *AB* is *L* and *AD* is *L*/2. Other porous media can be generated by adding more solid particles in this rectangle and maintaining the same porosity. After normalization, the coordinates of the four corners A, B, C, and D are (−0.5, 0), (0.5, 0), (0.5, 0.5), and (−0.5, 0.5), respectively.

parallel to each other and most importantly far from being straight. To quantify this effect a dimensionless parameter called hydraulic tortuosity of preferential flow paths $T$ is introduced. Tortuosity is defined as the ratio of the average length of microscopic flow paths to the length of the medium in the direction of macroscopic flux $L$ (Duda et al., 2011; Matyka et al., 2008). It is computed herein as a volume integral based on the simplified method (Duda et al., 2011) for low-Reynolds number flows:

$$T_i = \frac{\langle u \rangle}{\langle u_i \rangle}, \tag{7}$$

in which $\langle ... \rangle$ denotes a spatial average and $i$ is the direction parallel to the macroscopic flow. Second, the gas permeability is significantly affected by the surface area. Thus, the specific surface area $S$, which is defined as the ratio of the total interstitial surface area to the total volume of the fluid phase (ratio of the perimeter to the total area in 2D), is also computed. Generally, the boost of both tortuosity and specific surface area obstructs the flow, resulting in lower permeability. Third, shale formations are anisotropic due to the orientation of mineral foliations and laminated bedding planes. This leads to the description of their macroscopic physical properties, e.g. tortuosity and permeability as tensors rather than scalars. For this reason, both statistically isotropic and anisotropic geometries are produced to evaluate the directional dependency of their properties, computed in the two main orthogonal directions. Off-diagonal permeability elements are not considered in this study since their magnitude is reported to be significantly low (Ghanbarian and Javadpour, 2017; Guibert et al., 2015).

The parameter $D_i$ is responsible for the degree of anisotropy in the geometries generated using the QSGS method. In order to obtain isotropic structures, uniform main ($D_{1-4}$) and diagonal ($D_{5-8}$) growth probabilities must be set, with $D_{1-4}$: $D_{5-8} = 4$. By changing the ratio between horizontal and vertical probabilities (hereinafter referred to as the aspect ratio $AR = D_{1,3}/D_{2,4}$) anisotropy can be adjusted accordingly. The anisotropy factor for the intrinsic permeability $r = k_{min}/k_{max}$ is reported (Guibert et al., 2015) to have a large range of possible values in various sandstones and thus it is also studied in the present work.

### 3.2. Intrinsic permeability results

Several micro-porous media structures are generated to investigate the impact of the variation of the morphological features on the intrinsic permeability. In all the produced geometries the final porosity is slightly smaller than the nominal. As previously mentioned, ten geometries are produced for every set of parameters and simulations are performed for flow in both the horizontal ($x$) and vertical ($y$) direction to account for the possible anisotropy. In some of the following graphs, for each configuration, the mean value of the computed quantity is shown, while in others all the values are displayed in scatter plots for better visualization of their deviation. The permeability (both intrinsic and apparent) appearing in the graphs and the equations below is given in its non-dimensional form, by dividing its value with the square of the length of the computational domain in the streamwise direction ($L^2$).

To begin with, Fig. 3 for p shows the effect of porosity change on physical properties. The results are based on flow simulations on porous media with nominal porosities varying from 0.5 to 0.9 and fixed core distribution probability $c_d = 0.001$ and aspect ratio $AR = 1$ (sample structures are shown in the first row of Fig. 1). It should be noted that for this set of parameters, the porosity $\varepsilon = 0.45$ is the percolation threshold, i.e. the lowest porosity where the fluid is allowed to flow. For lower porosities permeability vanishes. It can be observed that the final porosity is smaller than the nominal up to almost 6% with decreasing porosity. Furthermore, when the value of the core distribution probability is fixed, the specific surface area and tortuosity decrease with the porosity, leading to higher permeability. Tortuosity and permeability in both flow directions seem to have close, almost overlapping values especially for high porosities. This is reasonable, since the geometries are generated to be statistically isotropic and at high porosities nearly each obstacle constitutes a separate island. However, near the percolation threshold isotropy is disrupted due to the many overlapping particles which change their aspect ratio. It can be also observed that the slope of permeability for low porosities is different compared to higher ones.

The scatter plots in Fig. 3 for p reveal the heteroscedasticity of the data, meaning that the variation of $T$ or $k$ differs depending on the value of porosity. Nevertheless, a general trend can be observed; small values of porosity yield a large scatter in the tortuosity $T$ and thus the permeability $k$, while the opposite happens for large porosities. An explanation for the large scatter could be that for porosities close to the percolation threshold particles overlap in random ways for each geometry and this creates different flow paths. Consequently, tortuosity can vary significantly even for the same value of porosity, leading to great discrepancies in permeability.

In addition to the porosity, the impact of the core distribution probability $c_d$ variation (sample structures are shown in the second row of Fig. 1) while the other two parameters are fixed ($\varepsilon = 0.7$ and $AR = 1$) is also studied. The results are presented in Fig. 4. By increasing $c_d$ the number of particles rises, their size is reduced and therefore these geometries tend to become homogeneous. This fact is reflected on both tortuosity and permeability curves, whose components happen to almost coincide in both directions. Through these graphs, it is apparent that the drop of grain size (roughly described by the mean diameter $D$) leads to significant permeability decline, mostly due to the increment of the specific surface area, since the porosity is the same and the tortuosity changes only a little in this case.

Finally, the third factor taken into consideration is the degree of anisotropy (sample structures are shown in the third row of Fig. 1). The generated micro-porous media are produced by maintaining $\varepsilon = 0.7$ and $c_d = 0.001$. Flow simulations are performed both in $x$ direction, where the directional growth probability is larger, and in $y$ direction. Based on the graphs shown in Fig. 5 the enlargement of the specific surface area and more importantly of tortuosity leads to a serious decline of the permeability $k_y$. This is due to the obstacles having a large height to width ratio, exerting more resistance to the flow and obstructing many flow paths.

In the $x$ direction where the particles are more stretched, by decreasing the height to width ratio, (increasing $AR$) flow paths tend to become less sinuous, nearly horizontal, and as a consequence, the tortuosity approaches unity. However, as increasing $S$ reduces permeability, from Fig. 5b it is found that $k_x$ does not grow monotonically as expected, remaining though in the same order of magnitude. This is due to the competition between the favourable $T$ and the unfavourable $S$. Initially, the beneficial impact of tortuosity dominates, however as the particles become more stretched and $S$ increases, again they exert more resistance to the flow blocking passages and leading to a drop of permeability. The peak of the $k_x$ curve for these simulated anisotropic QSGS structures is observed to be at $AR = 50$. Finally, the anisotropy factor $r$ varies from 0.95 for the statistically isotropic geometry (less anisotropic porous medium) to 0.03 for the most anisotropic samples for the $AR$ region considered.

### 3.3. Intrinsic permeability formulation

In this section we consider how to fit the intrinsic permeability of the 2D geometries generated by the QSGS algorithm, utilizing analytical expressions. Dimensional analysis suggests that Darcy permeability is a function of the porosity $\varepsilon$, tortuosity $T$, and specific surface area $S$. One of the most well-known permeability correlations, initially developed by Kozeny and later modified by Carman, is the following semi-empirical formula

$$k = \frac{\varepsilon^3}{cT^2(1-\varepsilon)^2 S^2}, \tag{8}$$

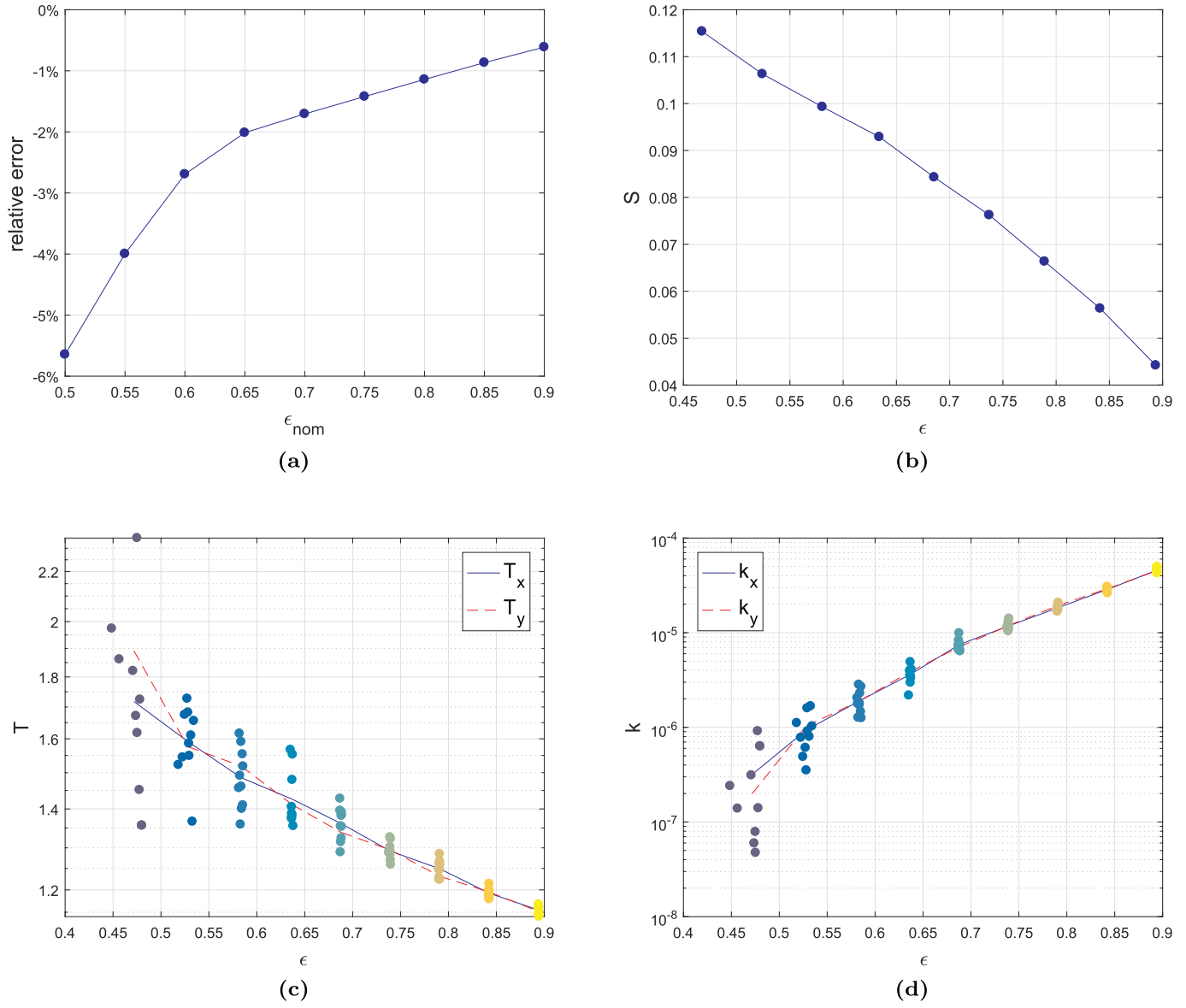


**Fig. 3.** Numerical results for geometries with the core distribution probability $c_d = 0.001$ and aspect ratio $AR = 1$. Variation of the relative error of the final porosity $\varepsilon$ with the nominal porosity and variation of the specific surface area $S$ with $\varepsilon$ in the first row. Variation of the tortuosity $T$ and permeability $k$ in the second row; the data points refer to $k_x$ and $T_x$, respectively. The trend of the properties in the $x$ direction is indicated with a solid line, while in the $y$ direction a dashed line is used.

where $c$ is the Kozeny-Carman (KC) coefficient or otherwise stated as shape factor. The above formulation was derived under the assumption that the porous medium is consisted of a bundle of capillaries of fixed cross-sectional shape. The KC expression is widely used for various 2D and 3D porous media (Chen et al., 2015a; Nabovati and Sousa, 2007).

A vast number of researchers, inspired by the work of Kozeny, have established correlations of permeability for different types of porous media. However, they require numerical or experimental data to derive the values of the fitting parameters. The essential derivation of a permeability-porosity relationship of mudrocks is a challenging task due to the complexity of the morphological features of these ultra-tight porous media (Chen et al., 2015a). In this study, this problem is addressed by fitting the tortuosity and permeability using the aforementioned independent variables i.e. porosity $\varepsilon$, core distribution probability $c_d$, and aspect ratio $AR$.

### 3.3.1. Isotropic geometries

In order to derive an accurate model for the intrinsic permeability of isotropic geometries ($AR = 1$), several QSGS structures are generated; specifically for $c_d = 0.001, 0.005, 0.01$ and porosities ranging from the vicinity of the percolation threshold, to $\varepsilon = 0.9$. At this point, it should be noted that increasing $c_d$ and consequently the number of solid islands, leads to the percolation threshold being at a higher porosity. Simultaneously, since the solid islands are smaller and thus less likely to overlap, the permeability $k$ and tortuosity $T$ are less heteroscedastic.

The first step to derive a similar formulation is the generalization of tortuosity as a function of the independent parameters that determine the structure, i.e. $\varepsilon$ and $c_d$. Based on the numerical simulations on 2D porous matrices of freely overlapping square particles, where several established expressions for tortuosity were tested, the tortuosity correlation providing the best fit was $T = 1 - a_1 \ln(\varepsilon)$, where $a_1$ is a fitting parameter (Comiti and Renaud, 1989; Matyka et al., 2008). This expression is thus used in the present study as a starting point for the correlation of $T = f(\varepsilon, c_d)$. The relevant tortuosity data and appropriate fitting (as seen in Fig. 6a) result in a formulation of the following form

$$T = 1 - a_1 c_d^{a_2} \ln(\varepsilon), \tag{9}$$

where $a_1 = 2$ and $a_2 = 0.11$.

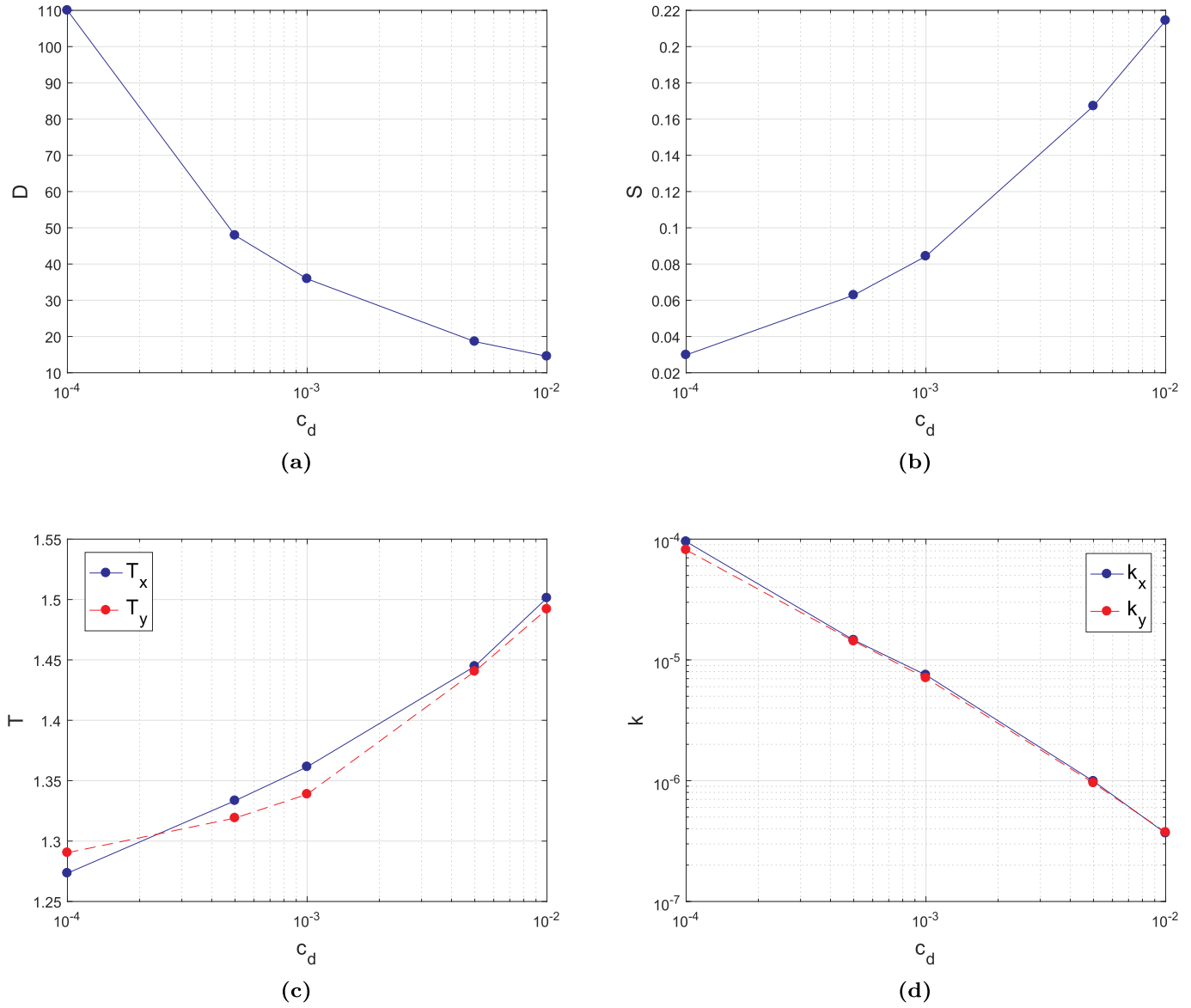


**Fig. 4.** Numerical results for geometries with the porosity $\varepsilon = 0.7$ and aspect ratio $AR = 1$. Variation of the mean diameter $D$ and specific surface area $S$ with the core distribution probability $c_d$ in the first row. Variation of the tortuosity $T$ and permeability $k$ with $c_d$ in the second row. The trend of the properties in the $x$ direction is indicated with a solid line, while in the $y$ direction a dashed line is used.

Considering the two-dimensional porous medium as a periodic array of circular discs with radius $R$, as in the first schematic diagram in Fig. 2, the analytical formula for permeability, which is accurate for high porosities, reads (Chai et al., 2011).

$$k_{in,c} = \frac{1}{8\pi}\left[-\ln P - \frac{3}{2} + 2P - \frac{P^2}{2}\right], \tag{10}$$

where $P = 1 - \varepsilon$ stands for the solid fraction and $\varepsilon = 1 - \pi R^2/L^2$.

More complex porous media can be generated by replacing the cylinder with numerous solid particles as shown in the last two schematics of Fig. 2 (Wu et al., 2017a). While keeping the same porosity, the analytical formula could be used although certain modifications would be imperative. To begin with, in order to use the analytical model which is based on a regularly ordered medium of high porosity to evaluate the tested structures of randomly placed and often overlapping particles, the effect of the tortuous flow paths should be considered utilizing the factor $T^{-2}$. This factor influences the slope of the permeability curve. Apart from this, the number of solid islands, which affects the permeability as discussed previously, should also be taken into account. This reasoning yields the following fitting formula

$$k_{in,random,is} = \frac{k_{in,c}}{a_3 n T^2}, \tag{11}$$

where the factor $n = N_x N_y c_d$ refers to the nominal number of solid islands and $a_3$ is an adjustable parameter. The physical meaning of $a_3$ reflects the impact of the particles' shape.

Suitable fitting yields $a_3 = 0.7$ and the related curves are shown in Fig. 6b. The fitting of the tortuosity is less accurate for high porosities. On the other hand, as expected, the fitting of the permeability is satisfactory for high porosities but the permeability is overestimated close to the percolation threshold, especially for geometries with low $c_d$ which are more heterogeneous.

### 3.3.2. *Anisotropic geometries*

It is of central importance to extend and revise the permeability expression to include anisotropic structures, since the shale matrix can be highly anisotropic. To this end, further anisotropic geometries are generated for several porosities ranging from the vicinity of the

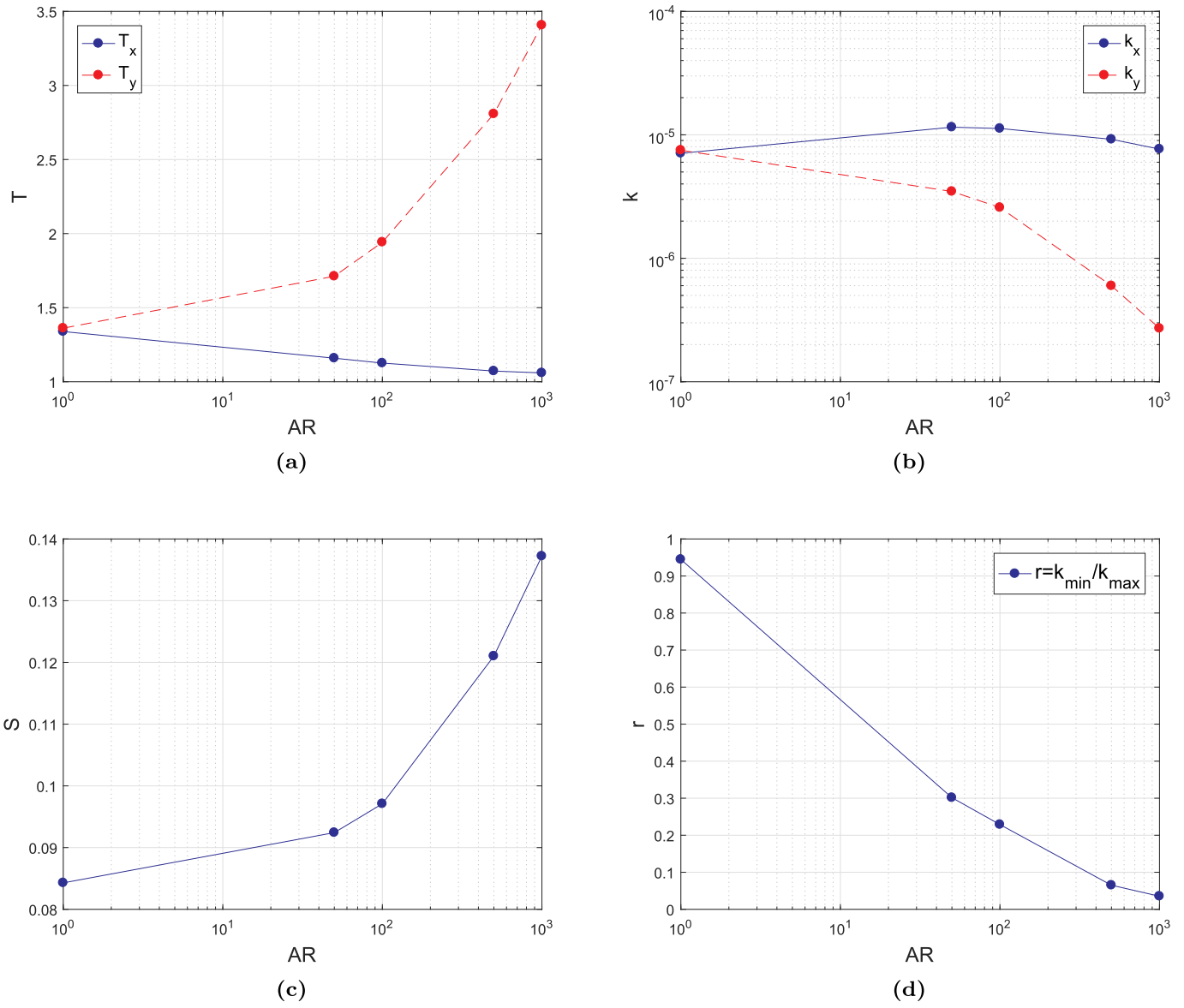


**Fig. 5.** Numerical results for geometries with porosity $\varepsilon = 0.7$ and core distribution probability $c_d = 0.001$. Variation of tortuosity $T$ and permeability $k$ with aspect ratio $AR$ in the first row. Variation of specific surface area $S$ and anisotropy factor $r$ with $AR$ in the second row. The trend of the properties in $x$ direction is indicated with a solid line, while in $y$, a dashed line is used.

percolation threshold, to $\varepsilon = 0.9$, while the core distribution probability is fixed at $c_d = 0.001$ and the aspect ratio $AR = 100$ or 1000. In Fig. 7 their simulation results are compared with those of the corresponding (for the same $c_d$) isotropic geometries and appropriate fitting is applied. It is obvious that the effect of the elongation of the solid islands is more pronounced for lower porosities, where the tortuosity is highly increased and the permeability is severely attenuated.

The tortuosity is fitted with the same equation as in the isotropic cases but adding the contribution of $AR$ as follows

$$T = 1 - a_1 c_d^{a_2} AR^{a_5} \ln(\varepsilon), \tag{12}$$

where $a_2 = 0.11$ as previously fitted. In the direction of the elongation of the islands ($x$) the flow is facilitated, the tortuosity approaches unity and $a_1 = 8.8$ while $a_5 = -0.48$. In the perpendicular direction ($y$), we obtain $a_1 = 0.5$ and $a_5 = 0.48$.

The correct approximation of tortuosity allows the estimation of permeability utilizing the same expression as in isotropic geometries, with the exception that the adjustable parameter $a_3$ changes significantly. This modification is necessary since the analytical expression in Eq. (10) is derived for cylindrical discs, while in the anisotropic structures solid islands are far from being so. The degree of anisotropy $AR$ is also taken into account and the resulting formula reads

$$k_{in,random,an} = \frac{k_{in,c}}{a_3 n AR^{a_4} T^2}. \tag{13}$$

In anisotropic structures, the particles' shape is more ellipsoidal and hence, the particles are less likely to overlap. Thus fitting yields $a_3 = 0.3$. The exponent $a_4$ is adjusted according to the direction of the flow. For the computation of permeability in the $x$ direction $a_4 = 0.17$ while in the $y$ direction, $a_4 = 0.31$. The fitted formulation is shown in Fig. 7, where we can observe that even though the fitting of tortuosity is not ideal, the permeability formulation yields a good approximation of the actual permeability, especially for high porosities.

To conclude, Eq. (13) models the intrinsic permeability for both

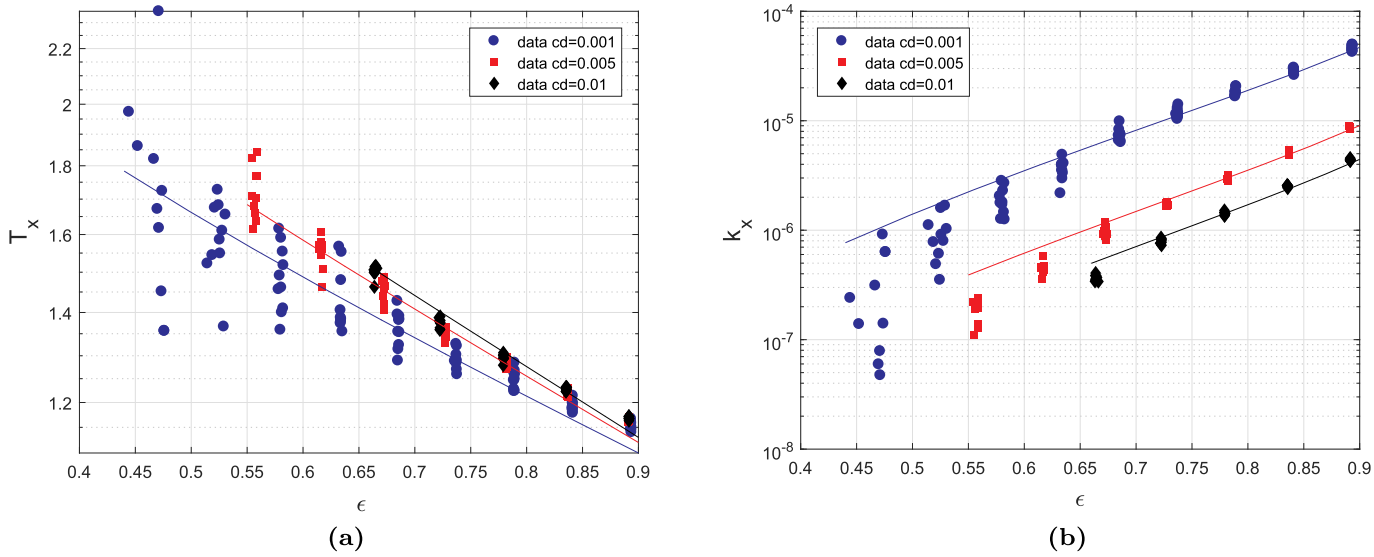


**Fig. 6.** Intrinsic permeability formulation for isotropic geometries. Fitting tortuosity with equation (9) and the permeability with equation (11).

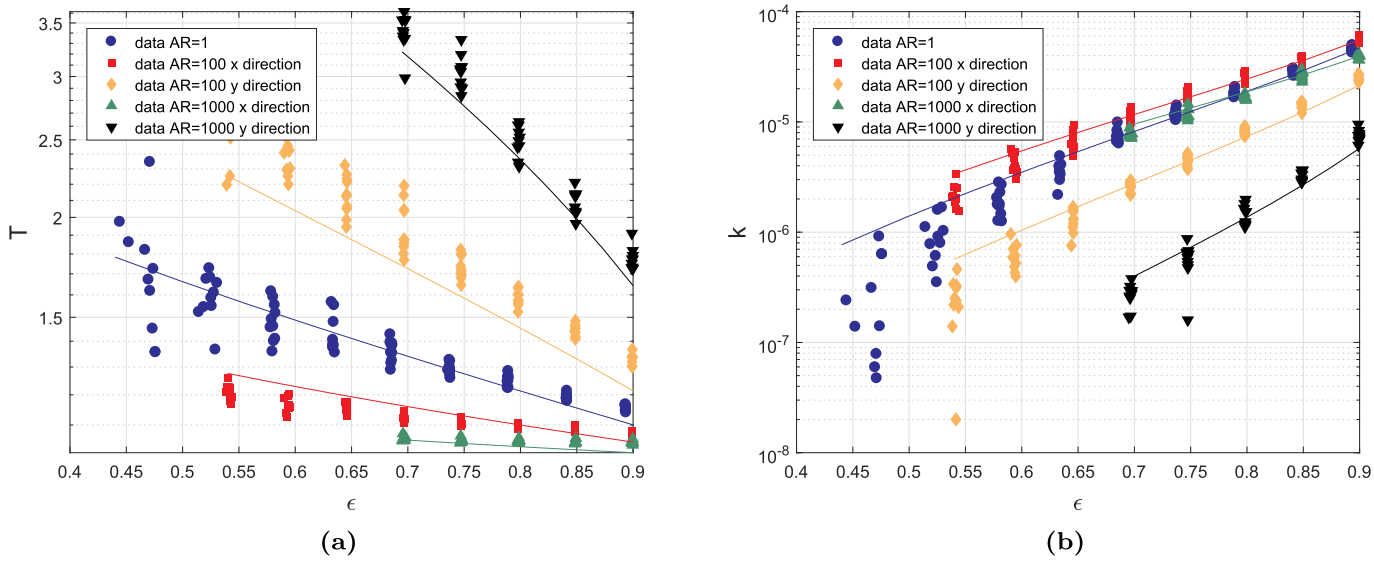


**Fig. 7.** Intrinsic permeability formulation for both isotropic and anisotropic geometries with core distribution probability $c_d = 0.001$. Fitting of tortuosity with equation (12) and permeability with equation (13).

isotropic ($AR = 1$) and anisotropic QSGS structures, requiring the calculation of the tortuosity using Eq. (12) anisotropic. The above equations depend only on the independent variables ε, $c_d$ and $AR$ and their coefficients are fixed according to the above cases. As a result, this permeability formulation includes five fitting parameters, which unlike others in the literature are the same regardless of particle shape and size. Table 1 summarizes the aforementioned coefficients for each case. Consequently, intrinsic permeability estimation for random two-dimensional porous media generated by the QSGS method is straightforward since it does not entail any numerical simulations.

**Table 1**
Fitting coefficients for intrinsic permeability formulation Eqs. (12) and (13).

| Structure | Flow direction | $a_1$ | $a_2$ | $a_3$ | $a_4$ | $a_5$ |
|---|---|---|---|---|---|---|
| Isotropic | any | 2 | 0.11 | 0.7 | – | – |
| Anisotropic | $x$ | 8.8 | 0.11 | 0.3 | 0.17 | −0.48 |
| | $y$ | 0.5 | 0.11 | 0.3 | 0.31 | 0.48 |

## 4. Apparent permeability

### 4.1. Apparent permeability results

The various morphological features of the aforementioned two-dimensional complex porous media, unambiguously affect the apparent gas permeability. Numerical results of the linearized BGK solved by the DVM reveal the relationships between the controlling parameters of the QSGS structures and the apparent permeability. Due to the high computational cost (Ho et al., 2019), numerical results of only four porous structures are compared across a wide range of $Kn$ numbers. Nevertheless, these simulations are adequate to demonstrate the impact of the variation of each parameter on the apparent permeability, compared to a reference case. Simulations are performed for part of the slip and transition flow regimes which are of main interest as far as shale production is concerned. In Fig. 8 the data points represent the raw data and not mean values, since only one geometry is simulated for every set of QSGS parameters. The slip-corrected permeability, obtained by fitting the numerical solution of the NSEs imposing a first-order velocity-slip boundary condition (FVBC) at small Knudsen numbers to the first-

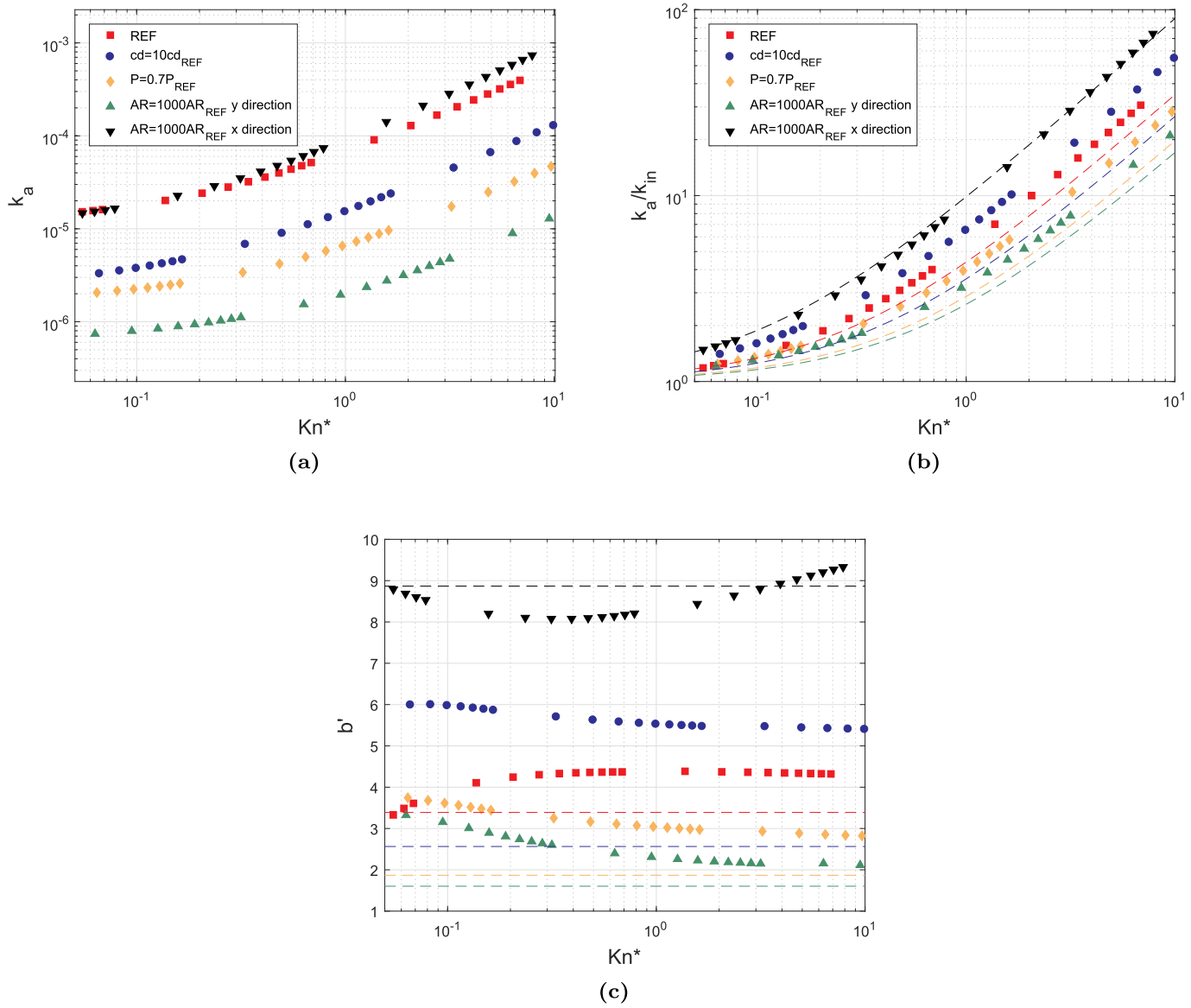


**Fig. 8.** Numerical results of the DVM for (a) the apparent gas permeability, (b) the ratio of the apparent permeability to the intrinsic, and (c) the slip factor, as a function of the effective Knudsen number $Kn^*$. Case 1, taken as reference shown in red squares, corresponds to a structure with the porosity $\varepsilon = 0.7$, core distribution probability $c_d = 0.001$, and aspect ratio $AR = 1$. For case 2 shown in blue circles, $c_d = 10c_{d_{ref}}$, while for case 3, in yellow diamonds, $\varepsilon = 0.7\varepsilon_{ref}$. Finally, cases 4 (in green upward-pointing triangle) and 5 (in black downward-pointing triangle) are the same structure having $AR = 1000AR_{ref}$ where the flow is in the $y$ and $x$ direction respectively. The dashed lines indicated with the same color as the corresponding cases are the slip-corrected permeability, derived from the numerical solution of the NSEs coupled with the FVBC. Note that the effective Kn number $Kn^*$ is 69,166,162,316,78 times of $Kn$ for the cases 1,2,3,4,5, respectively.

order of $Kn$, is also shown for comparison (Wu et al., 2017a). For low $Kn$ numbers, the NSEs with FVBC are solved instead of the BGK equations to reduce the computational cost. The DVM method requires further refinement of the spatial grids in the early slip regime and thus, the NSEs are preferred.

Specifically, the reference case 1 is a porous medium with $\varepsilon = 0.7$, $c_d = 0.001$ and $AR = 1$ (structure in Fig. 1c). The other three structures are generated by changing one of these parameters at a time. Firstly, for case 2, the core distribution probability $c_d$ is augmented ($c_d = 10c_{d_{ref}}$), then for case 3 the porosity is decreased ($\varepsilon = 0.7p_{ref}$), and finally a highly anisotropic structure ($AR = 1000AR_{ref}$) is generated for case 4 (structures in Fig. 1a, f and 1i respectively). Cases 4 and 5 share the same structure, however, for the former, pressure gradient is applied along the $y$ direction, while for the latter, it is applied on the $x$ direction.

The size of the pores in the simulated structures can be significantly smaller than the size of the computational domain in the direction of the flow ($L$). Therefore, the effective characteristic flow length to be used in the calculation of Knudsen number is not ($L$), but an effective pore size ($L^*$) determined by the expression (Wu et al., 2017a) as follows

$$L^* = L\sqrt{\frac{12k_{in}}{\varepsilon}}, \tag{14}$$

resulting in the effective Knudsen number to be calculated accordingly as

$$Kn^* = \frac{\lambda}{L^*} = Kn\sqrt{\frac{\varepsilon}{12k_{in}}}. \tag{15}$$

According to Klinkenberg's first observations, the permeability in low permeable porous media increases with the reciprocal of gas mean pressure. With the help of Eqs. (3) and (15) Klinkenberg's famous Eq. (4) can be rewritten as (Klinkenberg, 1941).

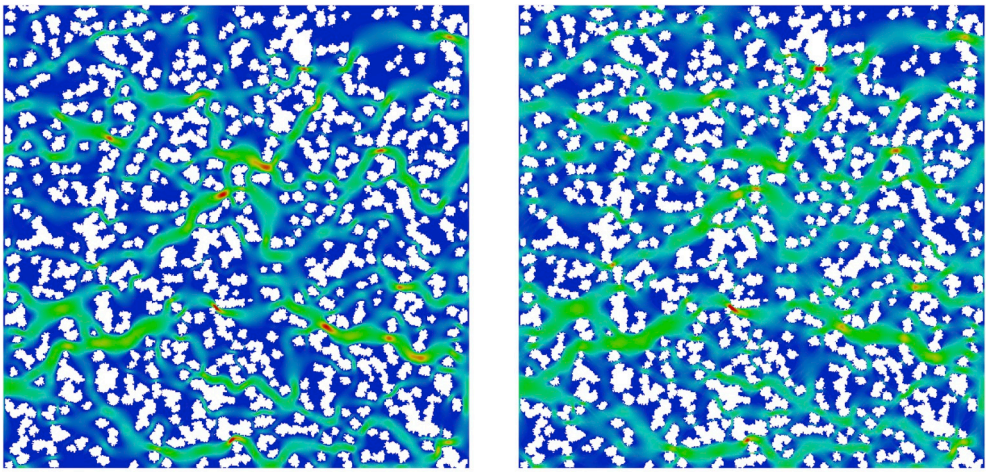

(a) $Kn^* = 0.007$ (b) $Kn^* = 0.7$

**Fig. 9.** Contour plots of the velocity magnitude normalized by its maximum value. The values increase from blue to red. The flow on the right plot has a $Kn^*$ number 100 times larger than the flow on the left. For larger $Kn^*$ number, the flow in the biggest pores is attenuated while it is enhanced in the smaller ones. It can be observed, hence, that the increment of rarefaction leads to a more homogeneous distribution of velocity. In other words, the effect of the high resistance of small pores tends to be eliminated resulting in a more uniform flow behaviour.

$$\frac{k_a}{k_{in}} = 1 + b' Kn^*, \tag{16}$$

where $b'$ is the "equivalent slip factor".

The velocity distribution contour plots of the reference case in Fig. 9 give useful insight of the rarefaction effects. A first observation for large $Kn^*$ numbers is that the flow is more uniformly distributed along more paths. Moreover, the dimensionless velocity in large pores is attenuated. At the same time, in many of the smaller pores, the dimensionless velocity is significantly enhanced due to the large velocity slip at the solid surfaces. Therefore, the difference of flow resistances for pores of different sizes tends to be eliminated and thus the flow becomes more uniform. Quantitatively speaking, for $Kn^* = 0.007$, 39% of the cells have velocity magnitude greater than the mean value, while for $Kn^* = 0.7$, this percentage increases to 42%. Additionally, in the former case 83% of the cells have velocity magnitude greater than the one tenth of the mean value, while the same percentage increases to 90% in the latter case. As a consequence, increasing rarefaction reduces the impact of heterogeneity.

The graph in Fig. 8a indicates that, generally speaking, the apparent permeability follows a similar trend as the intrinsic one, i.e. increase of $c_d$, decrease of porosity and increase of height to width ratio of the particles all lead to a drop of permeability. At the same time, $k_{in_1} > k_{in_5} > k_{in_2} > k_{in_3} > k_{in_4}$ and $k_{a_1} > k_{a_5} > k_{a_2} > k_{a_3} > k_{a_4}$. However, for cases 1 and 5 specifically, although $k_{in_1} > k_{in_5}$, $k_{a_1} > k_{a_5}$ is valid for low $Kn^*$ numbers ($Kn \leq 0.1$), then the inequality changes.

On the other hand, Fig. 8b demonstrates a different tendency of the permeability enhancement ($k_a/k_{in}$) in the regimes shown. In particular, for case 2 the opposite trend is observed between permeability enhancement and apparent permeability, i.e. $k_{a_2}/k_{in_2} > k_{a_1}/k_{in_1}$ even though $k_{a_1} > k_{a_2}$. However, for cases 3 and 4 the same trend is observed, i.e. $k_{a_1}/k_{in_1} > k_{a_3}/k_{in_3} > k_{a_4}/k_{in_4}$ while $k_{a_1} > k_{a_3} > k_{a_4}$. Finally, $k_{a_5}/k_{in_5} > k_{a_2}/k_{in_2} > k_{a_1}/k_{in_1}$ in the whole range of $Kn$ numbers shown.

The slip-corrected permeability generally underestimates the apparent permeability, with the exception of the low-tortuosity geometry (case 5). Consequently it should only be considered as accurate for very low $Kn^*$ numbers (even partially covering the slip regime). In addition to that, the effect of permeability enhancement being higher when increasing $c_d$ (i.e. the number of particles) for high $Kn^*$ numbers is not captured under the continuum assumption.

Therefore, increasing the core distribution probability $c_d$ leads to a boost of the apparent permeability with a rate higher than of the rest three cases (1,3,4). This means that the smaller the particles' size for the same porosity (thus smaller pores), the more apparent permeability is favoured. Moreover, introduction of anisotropy, where the flow is in the direction of the particles' elongation and tortuosity is low, leads to greater permeability enhancement than all the other cases for all $Kn^*$ numbers. This means that anisotropy not only favours apparent permeability compared to isotropic structures with the same nominal number of particles, but also compared to isotropic structures with smaller particles (cases 1,2) respectively.

On the contrary, drop of porosity and introduction of anisotropy where the flow is in the direction perpendicular to the particles' elongation, generally reduce the slope of $k_a$. As far as porosity is concerned, based on the analytical solution of Chai et al. (2011), which is valid for high porosity porous media in the slip regime, $k_a/k_{in}$ is expected to be higher for reduced porosities. The numerical results of DVM are in agreement with this tendency for $Kn^* \leq 0.07$. However, the numerical results of the NSEs coupled with FVBC do not confirm this. Additionally, for higher $Kn^*$ DVM results drop of porosity has a negative effect on permeability enhancement. Therefore, this trend indicated by the analytical formula is not verified by the numerical simulations on the various QSGS geometries.

The variation of the equivalent slip factor $b'$ with respect to $Kn^*$, as presented in Fig. 8c, is quite different among the cases considered. The slip factor of geometries with high tortuosity, i.e. cases $1-4$, tends to attenuate when $Kn^*$ is high, while for case 5 where tortuosity approaches unity $b'$ initially drops, reaches a minimum and then rises in the free molecular flow regime. Again, the slip-corrected permeability underestimates the slip factor for the tortuous cases, while it gives a good approximation for the least tortuous case 5. It should be noted that the error of $b'$ is more pronounced for low $Kn^*$, due to its derivation, so

possible shortcomings can affect severely the result of this specific variable in the slip regime. Finally, the classification of flow regimes, mentioned in Section 1, is based on pipe flow experiments and thus, may vary for more complex geometries, as emphasized by Beskok and Karniadakis (1999). For this reason, as expected, the behaviour related to each flow regime is observed at different $Kn^*$ for each porous medium. Specifically, the range of $Kn^*$ with linear dependence between $Kn^*$ and $k_a$ indicates that slip behaviour can be observed roughly for $Kn^* \leq 0.06$, $Kn^* \leq 0.02$, $Kn^* \leq 0.02$, $Kn^* \leq 0.03$, $Kn^* \leq 0.06$ for the cases 1,2,3,4,5 respectively.

### 4.2. Apparent permeability formulation

Similar to the intrinsic permeability, the apparent permeability could also be expressed as a function of the independent variables. Additionally, it is a function of $Kn$. It is well-documented that $k_a$ is a linear function of $Kn$ in the slip regime for the diffuse gas-solid interaction (Wu et al., 2017a). Considering a periodic array of circular discs, as in Section 3.3, the analytical formula for the apparent gas permeability is a non-linear function of $Kn$ (Chai et al., 2011). Nevertheless, since the formula is based on the NSEs coupled with FVBC, its applicability is limited to the first-order of $Kn$. Therefore, by expanding the formula into a Taylor series around $Kn = 0$ and retaining up to the first-order terms, the accuracy is maintained for the slip regime (Wu et al., 2017a). This simplified expression reads

$$k_{a,c,slip} = k_{in,c} + 2\xi Kn \frac{1}{8\pi}\sqrt{\frac{\pi}{P}}(1 - 2P + P^2), \tag{17}$$

where $\xi = 1.15$ when the diffuse boundary condition is used, as in this study.

Dividing the above analytical formula by the factor $a_3 n A R^{a_4} T^2$, the first term turns into the general form of the intrinsic permeability $k_{in,random,an}$. The term proportional to $Kn$ needs to be adjusted accordingly, to incorporate the behaviour of the various QSGS structures in rarefied conditions, as explained in Section 4.1. For this reason, the factor $a_6 c_d^{a_7} AR^{a_8}$ is added. This yields

$$k_{a,random,an,slip} = k_{in,random,an} + 2\xi Kn \frac{1}{8\pi}\sqrt{\frac{\pi}{P}}(1 - 2P + P^2)\frac{a_6{}' c_d^{a_7{}'} AR^{a_8{}'}}{a_3 n A R^{a_4} T^2}, \tag{18}$$

$$\frac{k_{a,random,an,slip}}{k_{in,random,an}} = 1 + 2\xi Kn^* \frac{1}{8\pi}\sqrt{\frac{\pi}{P}}(1 - 2P + P^2)\frac{a_6 c_d^{a_7} AR^{a_8}}{k_{in,c}}, \tag{19}$$

where $AR = 1$ for isotropic geometries. The fitting is performed considering that the above semi-analytical expression is expected to be most accurate for high porosities. The numerical data utilized are derived from the NSEs coupled with the FVBC. The fitted curves are identical to the ones resulting from the corresponding numerical results (dashed lines) in Fig. 8b except for the case 3 which was not considered due to its low porosity.

It should be noted that the intrinsic permeability given by the semi-analytical model is a sufficient approximation of the intrinsic permeability of the simulated structures, mainly due to the large amount of geometries tested. The fitting for the apparent permeability is thus performed based on this approximation, but not accurate value. Unlike the fitting for the intrinsic permeability in Section 3.3, the simulated structures are fewer due to the high computational cost. It can be concluded then, that the coefficients of the formulae for estimation of the apparent permeability can be considered less reliable in this context. Nevertheless, using the resulted coefficients, we acquire a good indication of the dependency of the slip factor on ε, $c_d$ and $AR$ in the slip regime. The values of the coefficients that gave a satisfactory fit are shown in Table 2.

**Table 2**
List of fitting coefficients for apparent permeability formulation Eq. (19).

| Structure | Flow direction | $a_1$ | $a_2$ | $a_3$ | $a_4$ | $a_5$ | $a_6$ | $a_7$ | $a_8$ |
|---|---|---|---|---|---|---|---|---|---|
| Isotropic | any | 2 | 0.11 | 0.7 | – | – | 0.26 | −0.0091 | - |
| Anisotropic | $x$ | 8.8 | 0.11 | 0.3 | 0.17 | −0.48 | 0.26 | −0.0091 | 0.113 |
| | $y$ | 0.5 | 0.11 | 0.3 | 0.31 | 0.48 | 0.26 | −0.0091 | −0.113 |

## 5. Conclusions

In summary, the structural properties of porous media significantly affect not only the intrinsic permeability, but also the slip factor appearing in the apparent permeability, in different ways as analysed. This assertion is based on the numerical dataset produced from flow simulations of 400 geometries, generated using the QSGS method. This conclusion suggests that the use of permeability models based on over-simplifications of the complex porous media geometry, such as the consideration of the pores as straight tubes, gives misleading results. To address this issue, we presented a simple semi-analytical formulation to calculate the intrinsic permeability (Eq. (13)). This formulation was also extended and revised to capture the apparent permeability in the slip regime (Eq. (19)).

The proposed approach of permeability estimation is fast and efficient, since it does not entail numerical simulations or experimental measurements for the approximation of intrinsic and apparent gas permeability (in the slip regime). For the moment, this approximation is limited to 2D QSGS geometries. The physical features of real 3D porous media cannot be fully represented in such structures. Therefore, the validity of the current results and their extension in real porous media requires further investigation.

This study also highlights the uncertainties and challenges with regards to estimating the permeability of complex porous media through simplified formulae. Since random structures with the same nominal properties can have distinct permeabilities, the concept of a unified formulation is itself contradictory. However, the proposed models successfully capture the impact of the variation of morphological characteristics on the permeability, giving indicative estimates and trends. Last but not least, our numerical results could also serve as benchmarking cases to assist modelling of rarefied gas flows in complex geometries.

## Acknowledgments

This work is financially supported by the joint project from the Royal Society of Edinburgh and National Natural Science Foundation of China under Grant No. 51711530130, the Carnegie Research Incentive Grant for the Universities in Scotland, and the Engineering and Physical Sciences Research Council (EPSRC) in the UK under grants EP/M021475/1 and EP/R041938/1. The data of the 400 QSGS geometries within this publication can be freely accessed at http://dx.doi.org/10.17632/mdhxr976vg.1.

## References


Beskok, A., Karniadakis, G.E., 1999. Report: a model for flows in channels, pipes, and ducts at micro and nano scales. Microscale Thermophys. Eng. 3 (1), 43–77.

Bhatnagar, P.L., Gross, E.P., Krook, M., 1954. A model for collision processes in gases. I. Small amplitude processes in charged and neutral one-component systems. Phys. Rev. 94 (3), 511–525.

Chai, Z., Lu, J., Shi, B., Guo, Z., 2011. Gas slippage effect on the permeability of circular cylinders in a square array. Int. J. Heat Mass Tran. 54 (13–14), 3009–3014.

Chen, L., Fang, W., Kang, Q., De'Haven Hyman, J., Viswanathan, H.S., Tao, W.Q., 2015a. Generalized lattice Boltzmann model for flow through tight porous media with Klinkenberg's effect. Phys. Rev. E 91 (3), 033004.

Chen, L., Kang, Q., Dai, Z., Viswanathan, H.S., Tao, W., 2015b. Permeability prediction of shale matrix reconstructed using the elementary building block model. Fuel 160, 346–356.

Civan, F., 2010. Effective correlation of apparent gas permeability in tight porous media. Transport Porous Media 82 (2), 375–384.

Comiti, J., Renaud, M., 1989. A new model for determining mean structure parameters of fixed beds from pressure drop measurements: application to beds packed with parallelepipedal particles. Chem. Eng. Sci. 44 (7), 1539–1545.

Darabi, H., Ettehad, A., Javadpour, F., Sepehrnoori, K., 2012. Gas flow in ultra-tight shale strata. J. Fluid Mech. 710, 641–658.

Duda, A., Koza, Z., Matyka, M., 2011. Hydraulic tortuosity in arbitrary porous media flow. Phys. Rev. E 84 (3), 036319.

Gad-el Hak, M., 1999. The fluid mechanics of microdevices–the freeman scholar lecture. J. Fluid Eng. 121 (1), 5.

Ghanbarian, B., Javadpour, F., 2017. Upscaling pore pressure-dependent gas permeability in shales. J. Geophys. Res. Solid Earth 122 (4), 2541–2552.

Ghassemi, A., Pak, A., 2011. Pore scale study of permeability and tortuosity for flow through particulate media using Lattice Boltzmann method. Int. J. Numer. Anal. Methods GeoMech. 35 (8), 886–901.

Guibert, R., Nazarova, M., Horgue, P., Hamon, G., Creux, P., Debenest, G., 2015. Computational permeability determination from pore-scale imaging: sample size, mesh and method sensitivities. Transport Porous Media 107 (3), 641–656.

Ho, M.T., Zhu, L., Wu, L., Wang, P., Guo, Z., Li, Z.-H., Zhang, Y., 2019. A multi-level parallel solver for rarefied gas flows in porous media. Comput. Phys. Commun. 234, 14–25.

Holt, J.K., 2006. Fast mass transport through sub-2-nanometer carbon nanotubes. Science 312 (5776), 1034–1037.

Javadpour, F., 2009. Nanopores and apparent permeability of gas flow in mudrocks (shales and siltstone). J. Can. Pet. Technol. 48 (08), 16–21.

Kazmouz, S.J., Giusti, A., Mastorakos, E., 2016. Numerical simulation of shale gas flow in three-dimensional fractured porous media. J. Unconv. Oil Gas Resour 16, 90–112.

Klinkenberg, L.J., 1941. The permeability of porous media to liquids and gases. Am. Pet. Inst. 200–213.

Lin, D., Wang, J., Yuan, B., Shen, Y., 2017. Review on gas flow and recovery in unconventional porous rocks. Adv. Geo-energy Res. 1 (1), 39–53.

Matyka, M., Khalili, A., Koza, Z., 2008. Tortuosity-porosity relation in porous media flow. Phys. Rev. E 78 (2), 026306.

Maxwell, J.C., 1879. On stresses in rarified gases arising from inequalities of temperature. Phil. Trans. Roy. Soc. Lond. 170 (0), 231–256.

Nabovati, A., Sousa, A., 2007. Fluid flow simulation in random porous media at pore level using the Lattice Boltzmann Method. J. Eng. Sci. Technol. 2 (3), 226–237.

Ren, J., Guo, P., Peng, S., Yang, C., 2016. Investigation on permeability of shale matrix using the lattice Boltzmann method. J. Nat. Gas Sci. Eng. 29, 169–175.

Sharipov, F., Graur, I.A., 2012. Rarefied gas flow through a zigzag channel. Vacuum 86 (11), 1778–1782.

Singh, H., Javadpour, F., Ettehadtavakkol, A., Darabi, H., 2014. Nonempirical apparent permeability of shale. SPE Reservoir Eval. Eng. 17 (03), 414–424.

Su, W., Lindsay, S., Liu, H., Wu, L., 2017. Comparative study of the discrete velocity and lattice Boltzmann methods for rarefied gas flows through irregular channels. Phys. Rev. E 96 (2), 023309.

Varoutis, S., Naris, S., Hauer, V., Day, C., Valougeorgis, D., 2009. Computational and experimental study of gas flows through long channels of various cross sections in the whole range of the Knudsen number. J. Vac. Sci. Technol. 27 (1), 89–100.

Wang, J., Kang, Q., Wang, Y., Pawar, R., Rahman, S.S., 2017. Simulation of gas flow in micro-porous media with the regularized lattice Boltzmann method. Fuel 205, 232–246.

Wang, M., Wang, J., Pan, N., Chen, S., 2007. Mesoscopic predictions of the effective thermal conductivity for microscale random porous media. Phys. Rev. E 75 (3), 1–10.

Wu, L., Ho, M.T., Germanou, L., Gu, X.-J., Liu, C., Xu, K., Zhang, Y., 2017a. On the apparent permeability of porous media in rarefied gas flows. J. Fluid Mech. 822, 398–417.

Wu, T., Li, X., Zhao, J., Zhang, D., 2017b. Multiscale pore structure and its effect on gas transport in organic-rich shale. Water Resour. Res. 53 (7), 5438–5450.

Zhang, L., Li, D., Lu, D., Zhang, T., 2015. A new formulation of apparent permeability for gas transport in shale. J. Nat. Gas Sci. Eng. 23, 221–226.